Monitoring contractility in cardiac tissue with cellular resolution using bio-integrated microlasers

Marcel Schubert[1,*], Lewis Woolfson[1], Isla RM Barnard[1], Amy M Dorward[2], Becky Casement[1], Andrew Morton[1], Gavin B Robertson[2], Paul L Appleton[3], Gareth B Miles[4], Carl S Tucker[5], Samantha J Pitt[2], Malte C Gather[1,6*]

[1] SUPA, School of Physics and Astronomy, University of St Andrews

[2] School of Medicine, University of St Andrews

[3] School of Life Sciences, University of Dundee

[4] School of Psychology & Neuroscience, University of St Andrews

[5] The Queen's Medical Research Institute, University of Edinburgh

[6] present address: Centre for Nanobiophotonics, Department of Chemistry, Universität zu Köln

* ms293@st-andrews.ac.uk; mcg6@st-andrews.ac.uk

The contractility of cardiac cells is a key parameter describing the bio-mechanical characteristics of the beating heart, but functional monitoring of 3D cardiac tissue with single cell resolution remains a major challenge. Here, we introduce microscopic whispering gallery mode (WGM) lasers into cardiac cells to realize all-optical recording of transient cardiac contraction profiles with cellular resolution. The brilliant emission and high spectral sensitivity of microlasers to local changes in refractive index enable long-term tracking of individual cardiac cells, monitoring of drug administration, accurate measurements of organ scale contractility in live zebrafish, and robust contractility sensing through hundreds of micrometres of rat heart tissue. Our study reveals changes in sarcomeric protein density as an underlying factor to cardiac contraction. More broadly, the use of novel micro and nanoscopic lasers as non-invasive, bio-integrated optical sensors brings new opportunities to monitor a wide range of physiological parameters with cellular resolution.

An estimated 26 million patients suffer from heart failure worldwide, and further advances in cardiac regeneration depend critically on the ability to locally resolve the contractile properties of heart tissue[1,2]. Currently available techniques lack speed, sensitivity and single cell specificity, especially in deep tissue. To monitor cardiac contractility in isolated cells in a culture dish, transmission or fluorescence microscopy is often sufficient to track the distinct structural features of myofibrils[3], cellular organelles which comprise repeating contractile elements called sarcomeres. However, characterising contractility with adequate resolution in the more complex 3-dimensional structures of cardiac tissue remains a major challenge, both *in vitro* and *in vivo*, mainly due to the fast dynamics of contractions (<50 ms), the strong motion of the tissue and the severe scattering of light in tissue. Force transducers or soft strain gauge sensors have been developed, but their spatial resolution is very limited[4]. In transparent zebrafish, light sheet microscopes in combination with image reconstruction algorithms allow volumetric imaging of whole hearts with single cell resolution.[5] However, their resolution is too low to extract the contractility of single cells as this requires tracking nanometre changes in sarcomere spacing[2]. To achieve this resolution, fast intravital scanning confocal or multiphoton microscopes have been developed but the need for extensive image artefact removal by retrospective gating, active tissue stabilisation, and targeted fluorescent labelling means that so far they can only extract averaged contraction profiles. In addition, due to the inherent tissue dynamics, progress in achievable imaging depth has stalled at less than 100 μm from the heart surface[1,2,6,7], in strong contrast to functional imaging of the brain which has recently reached a depth of 850 μm[8].

To elucidate CM contractility under various experimental conditions, we explored the integration of WGM microlasers as multifunctional optical sensors. Chip-based fibre- and prism-coupled WGM biosensors have previously achieved sensitivities down to the single molecule and protein level[9,10]. However, their potential for intracellular sensing remains largely unexplored as integration into

50   biological systems requires further miniaturization, self-sustained and prolonged emission of light, and

51   data analysis protocols with improved robustness. Recently, microlasers were proposed as novel

52   optical tags to uniquely discriminate hundreds of thousands of cells[11–15].

53   **Intracellular refractive index sensing**

54   Fig. 1 illustrates the general principle of our laser-based contraction sensor. Brightly fluorescent

55   polystyrene microspheres with a diameter between 10 and 20 μm were used as efficient and robust

56   microscopic WGM lasers that show multi-mode emission under remote optical pumping[11]. These

57   lasers were actively internalized by different types of cardiac cells (Supplementary Fig. 1). Upon CM

58   contraction, individual peaks in the emission spectrum of the lasers showed a spectral red-shift

59   (typically, $\Delta\lambda \approx 50$ pm; Fig. 1d). Due to the bright and narrowband laser emission, the wavelength of

60   each lasing mode can be monitored rapidly (acquisition rate, 100 Hz) and accurately (spectral

61   resolution, 1 pm), revealing pulse-shaped perturbations in lasing wavelength synchronized across all

62   modes and coincident with the spontaneous contractions of the cell (Figs. 2a, 2b and Supplementary

63   Video 1). By tracking at least 2 pairs of TE and TM lasing modes and fitting their position to an optical

64   model, we independently determined the diameter *D* of each microsphere and the average external

65   refractive index n_{ext}, i.e. the refractive index (RI) of the volume probed by the evanescent component

66   of the WGM (Fig. 2c, Supplementary Fig. 2 and Supplementary Information). This revealed a

67   characteristic increase in RI during cell contractions. Statistical analysis of the microsphere diameter

68   was then applied to reduce the effect of fitting noise before reiterating the RI calculation. This

69   significantly improved the signal quality and thus allowed the detection of minute changes in n_{ext},

70   with a RI resolution of 5×10^{-5} (Supplementary Information), which rivals the most sensitive cell

71   refractometric techniques currently available[16].

72   Of the 2 pairs of TE and TM lasing modes required for fitting to the optical model, the brightest mode

73   typically has a lasing threshold well below 1 mJ/cm² (corresponding to <1 nJ/pulse, Fig. 2d). Above

74   threshold, this mode rapidly increased in intensity to become orders of magnitude more intense than

75   the background, which is mostly formed by bulk fluorescence of the microlaser (signal-to-background

76   ratio, SBR > 15dB). Single pulse excitation at around 1-2 mJ/cm^2 can be therefore used to accurately

77   determine the spectral position of this mode (Supplementary Fig. 3). By comparison, the least intense

78   mode of the 2 pairs required 10 to 50 times higher pump energy to pass the lasing threshold and to

79   determine its spectral position with sufficient accuracy to ensure convergence of our fitting algorithm.

80   Furthermore, we found that the periodic changes in RI due to cardiomyocyte contraction can be

81   utilized to determine the sensitivity (*S*) of each laser mode (Fig. 2e, Supplementary Fig. 4). Using *S* and

82   tracking the spectral position of just the brightest lasing mode then allows calculation of a linearly

83   approximated external refractive index n_{ext}^{*} , reducing the minimum required pump energy by at least

84 one order of magnitude. This calibration protocol enabled real time RI sensing, allowed continuous

85 yet non-disruptive read-out (Fig. 2f) and greatly improved the robustness of the approach under

86 challenging experimental conditions (see below).

87 Analysis of multiple CMs furthermore revealed that contractions consistently led to an increase of

88 cellular RI which indicates the presence of a reproducible physiological process that alters the optical

89 properties of CMs depending on the activation state of their contractile elements (Fig. 2g).

90 **Microlasers monitor myofibril contractility**

91 To identify the origin of the RI increase during CM contraction, we analysed the 3D organization of

92 myofibrils. It is generally assumed that CMs contract under isovolumetric conditions[17], yet X-ray

93 diffraction experiments have revealed a linear relationship between sarcomere length and volume of

94 the myofibril unit cell indicating that cell contractions significantly increase the protein density of the

95 myofibrils[18]. 3D reconstructions of cells showed that microlasers are surrounded by and in direct

96 contact with a dense network of myofibrils (Figs. 3a and 3b, Supplementary Fig. 5), indicating a strong

97 overlap of the contractile protein machinery with the evanescent field of the laser mode, which

98 typically extends up to 200 nm above the resonator surface. Cellular contractility in neonatal CMs was

99 then measured by staining sarcomeric actin filaments and tracking their length change during the

100 contraction cycle, while simultaneously recording spectral shifts in microlaser emission (Figs. 3c and

101 3d, and Supplementary Video 2). We find that the shortening in the sarcomere length (SL) of myofibrils

102 was linearly correlated to n_{ext} (Supplementary Fig. 6). In contrast, we did not observe spectral shifts

103 for microlasers located inside CMs that were not actively beating even when these were in direct

104 contact with a contracting neighbouring cell, confirming the very localized nature of evanescent field

105 sensing. This indicates that structural changes inside contracting myofibrils cause the red-shift in lasing

106 wavelength. Given that during systole n_{ext} increased by up to 0.003 and using the known protein

107 refractive index increment (dn/dc), we further estimated that the observed contraction-induced

108 changes in sarcomere length by about 10% led to a maximum increase in protein concentration of

109 approximately 8% (Supplementary Information). This finding is consistent with the previously

110 reported decrease in unit cell volume[18]. It does not contradict observations that the contraction of the

111 whole heart is isovolumetric; during contraction, cardiac cells are likely to expel water from the

112 myofibrils into different parts of the cell or to the extracellular space[19], causing a local increase in

113 myofibril density while still conserving the overall tissue volume. The effects associated with

114 sarcomeric lattice spacing and unit cell changes are of great importance for the function of cardiac

115 cells and are believed to play an important role in regulating the length-dependent activation of the

116 heart (Frank-Starling law). Since transient RI profiles provide a direct measure of CM contractility and

117 myofibril density, they provide new insights to the mechano-biology of cardiac cells. Importantly, the

118   signal monitored by the microlaser closely matches the contractility dynamics of nearby cells

119   (Supplementary Fig. 7, Supplementary Video 3) indicating that the functional properties of neonatal

120   CMs are not affected by the presence of the microlasers.

121   **Single cell barcoding**

122   As the microlaser size provides a unique label to identify and track individual cells over time

123   (Supplementary Fig. 8)[11], we were able to perform repeated monitoring of single neonatal CMs

124   (Fig. 4a). Normalized contractility profiles (Fig. 4b) showed high temporal regularity with minimal

125   beat-to-beat variations in pulse width (FWHM, Fig. 4c) and contraction time (t_{con}, Fig. 4d). For the

126   example in Fig. 4a, after 42 h, we observe the spontaneous transition into tachycardia which is

127   typically accompanied by increased myocardial tension at elevated beating rates (Bowditch effect), a

128   fundamental process underlying the force-frequency relationship of the heart[20]. At the cellular level,

129   this is caused by increased contractility, which we detected as a step-like increase in the maximum

130   and baseline n_{ext} (black arrow in Fig. 4a), allowing simple quantification of relative protein density

131   changes during the entire contraction cycle.

132   **Monitoring drug administration**

133   Next, we used the quantitative RI transient provided by our laser sensors to assess the effect of the

134   calcium channel blocker nifedipine (Fig. 4e). While the effect of nifedipine on voltage-gated Ca^{2+}-

135   channels and subsequent intracellular Ca^{2+} dynamics is well documented[21,22], the effect on

136   contractility is less well understood as it is difficult to access in neonatal and iPS-derived

137   cardiomyocytes. After administration of nifedipine and following a short period of adaptation,

138   spontaneously beating neonatal CMs showed strongly reduced contraction and relaxation speeds

139   (Fig. 4f,g). Furthermore, while we observed that nifedipine increased the pulse-to-pulse variability in

140   Δn_{ext}, the time to reach the maximum contraction changed only marginally (Fig. 4f). The lower

141   contraction speed was therefore largely caused by a reduced contractility of the cell. Under these

142   compromised conditions, the relationship between the mechanical dynamics (contraction speed) and

143   the maximum density change a cell can produce ($\Delta n_{ext,\,max}$) was linear (Fig. 4h, Supplementary Fig. 9).

144   The nanoscopic probe volume of microlasers and the quantitative contractility information they

145   provide therefore offer insights into fundamental bio-mechanical processes of cardiac cells, e.g.

146   revealing links between contractility, cross-bridge formation and mechano-transduction in individual

147   myofibrils (Supplementary Fig. 9).

148   **Simultaneous sensing of Calcium dynamics and contractility**

149   Microlaser contractility measurements can also be combined with all-optical electrophysiology

150   platforms[21,22]. Simultaneous laser spectroscopy and calcium imaging were performed on fully

151   differentiated mouse CMs that comprise highly organized myofibrils and a transverse tubular system

152 ensuring synchronized calcium release and rapid contraction throughout the cell (Figs. 5a and 5b,

153 Supplementary Video 4). Being non-phagocytic, adult CMs are not able to actively internalise

154 microlasers; so we instead measured spectral changes in the emission of microlasers that were in

155 contact with the cell membrane. Transient profiles of single adult CMs again showed contractions as

156 periodic increases in RI, albeit with smaller amplitude than before (Fig. 5c, Supplementary Fig. 10),

157 demonstrating that Δn_{ext} depends on the volume overlap of the evanescent component of the lasing

158 mode with the myofibrils. However, consistent with our previous observation, the RI transient showed

159 a direct correlation with sarcomere length (Fig. 5c), confirming a contraction-induced change in

160 myofibril density. We also compared the contractility profile to the profile of cytosolic Ca^{2+} and found

161 a characteristic latency time of 30 ms between calcium signalling and force development while the

162 maximum contraction speed coincided with peak Ca^{2+} concentration (Fig. 5c).

163 *In vivo* integration

164 Having demonstrated intra- and extracellular sensing *in vitro*, we next implemented our technique in

165 live zebrafish, a model organism with remarkable capabilities to repair and regenerate large fractions

166 of the heart[23]. Microlasers were injected by a microneedle (Fig. 5d), placing them at the outer wall of

167 the atrium (Figs. 5e and 5f). Extracellular sensing rather than direct intracellular injection was

168 performed to avoid disruption of the myocardium which at this developmental stage consists of a

169 single layer of cardiomyocytes that is not yet covered by the developing epicardium[24,25]. Lasing

170 wavelengths again showed the typical red-shift associated with cardiomyocyte contraction

171 (Supplementary Fig. 11). Due to increased tissue scattering and rapid movement (Supplementary

172 Video 5), the intensity of individual modes varied strongly, and the lower intensity TM modes were

173 not detected for a large fraction of the contraction cycle. However, after calibrating the sensitivity of

174 the microlaser from time-points that contained a sufficient number of modes (Supplementary Fig. 12;

175 c.f. Fig. 2d), we were able to construct complete contractility profiles for the beating zebrafish heart

176 (Fig. 5g). A measurement performed at a more posterior position of the atrium revealed a significantly

177 longer systolic plateau (Supplementary Fig. 13), demonstrating locally resolved contractility profiles

178 under *in vivo* conditions.

179 **Deep tissue contractility sensing**

180 Scattering of light in biological tissue severely limits the maximum depth at which optical imaging and

181 sensing can be performed. To explore the advantages of microlasers over conventional fluorescent

182 probes for deep tissue recording, we performed contractility sensing in preparations of thick,

183 electrically paced myocardial slices (Fig. 6a). With the ability to maintain functional, contractile heart

184 sections for several months, cardiac slices represent an increasingly important model system for drug

185 screening and for testing of novel cardiac regeneration approaches[26–28]. However, as their typical

186   thickness of 0.2 to 0.5 mm exceeds the scattering length of ballistic photons, single- and even multi-

187   photon microscopes fail to capture sub-cellular information from these slices. To illustrate this

188   limitation, we recorded two-photon microscopy stacks of heart muscle tissue (Fig. 6b). Although the

189   improved penetration depth at the excitation wavelength of 880 nm allows to image significantly

190   deeper than with conventional confocal microscopy, the image contrast degraded quickly with

191   increasing depth, making it impossible to resolve individual sarcomeres (typical spacing, 2 μm) or cell

192   contours beyond a depth of 100 μm. These results are in agreement with previously published

193   contractility studies where the requirement for fast and high-resolution sampling has so far prevented

194   imaging of cellular features in live heart tissue at depths greater than 100 μm[1,7].

195   To test if microlasers can sense contractility of cardiomyocytes at depths beyond the limit of current

196   microscopes, we applied them to a series of living myocardial slices with varying thickness between

197   100 and 400 μm (Fig. 6c). To improve light penetration, we changed to red-emitting lasers ($\lambda =$

198   610 nm) that are pumped by green light ($\lambda = 540$ nm). Although the signal decreased with increasing

199   tissue thickness, sufficient SBRs from 2 pairs of TE and TM modes were obtained to perform full RI

200   analysis even through 400 μm thick cardiac slices (Fig. 6d, Supplementary Fig. 14), i.e. at a depth that

201   was 4 times greater, than the maximum depth at which confocal and multiphoton microscopes can

202   still resolve sub-cellular features. Upon electrical pacing, the slices contracted reproducibly, inducing

203   clearly measurable changes in n_{ext} (Fig. 6e). From this data, we extracted high resolution contractility

204   profiles (Fig. 6f), comparable in quality and amplitude to those detected in isolated CMs (c.f. Fig. 5c).

205   **Discussion**

206   Restoring cardiac function after severe heart injury remains a major clinical challenge due to the low

207   capacity of the adult mammalian heart to grow new CMs[29]. Current regeneration approaches explore

208   the injection of CMs derived from human embryonic stem cells (hESC) or induced pluripotent stem

209   cells (hiPSC) into the injured heart and the growth of cardiac tissue *in vitro*[30–33]. Multifunctional probes

210   which monitor engineered cardiac tissue or the long-term integration of injected cells are urgently

211   needed. Chemical sensing with dye-based or transgenic calcium and voltage reporters are now

212   routinely used for all-optical electrophysiology[24,34]. However, despite their importance, these sensors

213   do not provide insights into the mechanical forces developed by the cells. The processes by which

214   engineered and native cardiac tissue couple mechanically therefore remain unknown[31,35]. Microlaser-

215   based contractility measurements fill this critical gap by monitoring the contractile properties of

216   individual cells during various developmental stages without the need for staining or genetic alteration.

217   Our spectroscopic contractility technique is also resilient to scattering compared to imaging-based

218   methods since scattering in biological tissue is elastic and hence does not alter spectral characteristics.

219   Furthermore, the nanosecond-pulsed pumping in combination with single-shot read-out applied here

220 virtually eliminates temporal averaging effects that represent a common source of motion artefacts

221 in intravital confocal or light sheet microscopy.[6] This can be combined with recent advances in

222 focussing of light deep into scattering tissue[36], to achieve remote and non-invasive monitoring of

223 cardiac function *in vivo*. For the example of cardiac slices shown here, the high sensitivity, bright

224 emission and single cell specificity of the microlasers leads to better performance at depth than

225 achievable with state-of-the-art microscopes. We expect that the application of novel microlaser

226 sources that are excited in the near-infrared transparency windows of biological tissue will enable a

227 dramatic further increase in sensing depth[37].

228 In the future, implementing our recently developed semiconductor WGM nanolasers[14], nanowire

229 lasers[38,39], or plasmonic nanolasers[40,41] will improve and simplify internalization further, eliminate any

230 mechanical restriction of the laser probes and drastically reduce the required pump energy. However,

231 surface passivation, heat management and advanced calibration protocols are needed for these single

232 mode lasers before a comparable degree of bio-compatibility and RI sensitivity can be achieved.

233 Furthermore, using high throughput chip-based devices[42] can enable massively parallel integration of

234 lasers into hiPSC- or hESC-derived cardiomyocytes which in turn would facilitate labelling and

235 monitoring of individual cells from the very early stages of the generation of functional cardiac tissue

236 onwards. Likewise, microlasers can offer functional sensing in newly developed stem cell therapies

237 that are able to restore infarcted tissue[43]. Moreover, techniques developed for ultra-sensitive

238 detection, including quantum-enhanced single molecule biosensing or frequency comb spectroscopy,

239 might be adopted to increase sensitivity and specificity of intracellular microlaser sensors even

240 further[44–46]. By providing single cell specificity, long-term tracking, and reduced sensitivity to scattering,

241 microlasers introduce new possibilities for translational approaches that extend well beyond current

242 microscopy-based techniques, offer reduced complexity, and impose fewer experimental restrictions.

243 **References**

244 1.   Aguirre, A. D., Vinegoni, C., Sebas, M. & Weissleder, R. Intravital imaging of cardiac function
245   at the single-cell level. *Proc. Natl. Acad. Sci.* **111**, 11257–11262 (2014).

246 2.   Kobirumaki-Shimozawa, F. *et al.* Nano-imaging of the beating mouse heart in vivo:
247   Importance of sarcomere dynamics, as opposed to sarcomere length per se, in the regulation
248   of cardiac function. *J. Gen. Physiol.* **147**, 53–62 (2016).

249 3.   Pasqualin, C. *et al.* SarcOptiM for ImageJ: high-frequency online sarcomere length computing
250   on stimulated cardiomyocytes. *Am. J. Physiol. Physiol.* **311**, C277–C283 (2016).

251 4.   Lind, J. U. *et al.* Instrumented cardiac microphysiological devices via multimaterial three-
252   dimensional printing. *Nat. Mater.* **16**, 303–308 (2016).

253 5.   Mickoleit, M. *et al.* High-resolution reconstruction of the beating zebrafish heart. *Nat.
254   Methods* **11**, 919–922 (2014).

255   6.   Vinegoni, C., Lee, S., Aguirre, A. D. & Weissleder, R. New techniques for motion-artifact-free
256   in vivo cardiac microscopy. *Front. Physiol.* **6**, 147 (2015).

257   7.   Matsuura, R. *et al.* Intravital imaging with two-photon microscopy reveals cellular dynamics in
258   the ischeamia-reperfused rat heart. *Sci. Rep.* **8**, 15991 (2018).

259   8.   Liu, R., Li, Z., Marvin, J. S. & Kleinfeld, D. Direct wavefront sensing enables functional imaging
260   of infragranular axons and spines. *Nat. Methods* **16**, 615–618 (2019).

261   9.   Vollmer, F. & Arnold, S. Whispering-gallery-mode biosensing: label-free detection down to
262   single molecules. *Nat. Methods* **5**, 591–596 (2008).

263   10.   Kim, E., Baaske, M. D., Schuldes, I., Wilsch, P. S. & Vollmer, F. Label-free optical detection of
264   single enzyme-reactant reactions and associated conformational changes. *Sci. Adv.* **3**,
265   e1603044 (2017).

266   11.   Schubert, M. *et al.* Lasing within Live Cells Containing Intracellular Optical Microresonators
267   for Barcode-Type Cell Tagging and Tracking. *Nano Lett.* **15**, 5647–5652 (2015).

268   12.   Humar, M. & Yun, S. H. Intracellular microlasers. *Nat. Photonics* **9**, 572–576 (2015).

269   13.   Schubert, M. *et al.* Lasing in Live Mitotic and Non-Phagocytic Cells by Efficient Delivery of
270   Microresonators. *Sci. Rep.* **7**, 40877 (2017).

271   14.   Fikouras, A. H. *et al.* Non-obstructive intracellular nanolasers. *Nat. Commun.* **9**, 4817 (2018).

272   15.   Martino, N. *et al.* Wavelength-encoded laser particles for massively multiplexed cell tagging.
273   *Nat. Photonics* **13**, 720–727 (2019).

274   16.   Liu, P. Y. *et al.* Cell refractive index for cell biology and disease diagnosis: past, present and
275   future. *Lab Chip* **16**, 634–644 (2016).

276   17.   Irving, T. C., Konhilas, J., Perry, D., Fischetti, R. & de Tombe, P. P. Myofilament lattice spacing
277   as a function of sarcomere length in isolated rat myocardium. *Am. J. Physiol. Circ. Physiol.*
278   **279**, H2568–H2573 (2000).

279   18.   Yagi, N. *et al.* Sarcomere-length dependence of lattice volume and radial mass transfer of
280   myosin cross-bridges in rat papillary muscle. *Pflugers Arch. Eur. J. Physiol.* **448**, 153–160
281   (2004).

282   19.   Moeendarbary, E. *et al.* The cytoplasm of living cells behaves as a poroelastic material. *Nat.*
283   *Mater.* **12**, 253–261 (2013).

284   20.   Schreckenberg, R. Endogenous Mechanisms for Regulating Myocardial Contractility. in
285   *Cardiomyocytes – Active Players in Cardiac Disease* 135–163 (Springer International
286   Publishing, 2016). doi:10.1007/978-3-319-31251-4_5.

287   21.   Klimas, A. *et al.* OptoDyCE as an automated system for high-throughput all-optical dynamic
288   cardiac electrophysiology. *Nat. Commun.* **7**, 11542 (2016).

289   22.   Dempsey, G. T. *et al.* Cardiotoxicity screening with simultaneous optogenetic pacing, voltage
290   imaging and calcium imaging. *J. Pharmacol. Toxicol. Methods* **81**, 240–250 (2016).

291   23.   Cao, J. & Poss, K. D. Explant culture of adult zebrafish hearts for epicardial regeneration
292   studies. *Nat. Protoc.* **11**, 872–881 (2016).

293   24.   Weber, M. *et al.* Cell-accurate optical mapping across the entire developing heart. *Elife* **6**,
294   e28307 (2017).

295 25. Brown, D., Samsa, L., Qian, L. & Liu, J. Advances in the Study of Heart Development and
296   Disease Using Zebrafish. *J. Cardiovasc. Dev. Dis.* **3**, 13 (2016).

297 26. Watson, S. A. *et al.* Preparation of viable adult ventricular myocardial slices from large and
298   small mammals. *Nat. Protoc.* **12**, 2623–2639 (2017).

299 27. Watson, S. A. *et al.* Biomimetic electromechanical stimulation to maintain adult myocardial
300   slices in vitro. *Nat. Commun.* **10**, 2168 (2019).

301 28. Fischer, C. *et al.* Long-term functional and structural preservation of precision-cut human
302   myocardium under continuous electromechanical stimulation in vitro. *Nat. Commun.* **10**, 117
303   (2019).

304 29. Vujic, A. *et al.* Exercise induces new cardiomyocyte generation in the adult mammalian heart.
305   *Nat. Commun.* **9**, 1659 (2018).

306 30. Tzahor, E. & Poss, K. D. Cardiac regeneration strategies: Staying young at heart. *Science
307   (80-.).* **356**, 1035–1039 (2017).

308 31. Shiba, Y. *et al.* Allogeneic transplantation of iPS cell-derived cardiomyocytes regenerates
309   primate hearts. *Nature* **538**, 388–391 (2016).

310 32. Ronaldson-Bouchard, K. *et al.* Advanced maturation of human cardiac tissue grown from
311   pluripotent stem cells. *Nature* **556**, 239–243 (2018).

312 33. Liu, Y.-W. *et al.* Human embryonic stem cell–derived cardiomyocytes restore function in
313   infarcted hearts of non-human primates. *Nat. Biotechnol.* **36**, 597–605 (2018).

314 34. Jones, J. S., Small, D. M. & Nishimura, N. In Vivo Calcium Imaging of Cardiomyocytes in the
315   Beating Mouse Heart With Multiphoton Microscopy. *Front. Physiol.* **9**, 969 (2018).

316 35. Gaetani, R. *et al.* Epicardial application of cardiac progenitor cells in a 3D-printed
317   gelatin/hyaluronic acid patch preserves cardiac function after myocardial infarction.
318   *Biomaterials* **61**, 339–348 (2015).

319 36. Jeong, S. *et al.* Focusing of light energy inside a scattering medium by controlling the time-
320   gated multiple light scattering. *Nat. Photonics* **12**, 277–283 (2018).

321 37. Fernandez-Bravo, A. *et al.* Continuous-wave upconverting nanoparticle microlasers. *Nat.
322   Nanotechnol.* **13**, 572–577 (2018).

323 38. Feng, C. *et al.* Organic-Nanowire–SiO 2 Core–Shell Microlasers with Highly Polarized and
324   Narrow Emissions for Biological Imaging. *ACS Appl. Mater. Interfaces* **9**, 7385–7391 (2017).

325 39. Wu, X. *et al.* Nanowire lasers as intracellular probes. *Nanoscale* **10**, 9729–9735 (2018).

326 40. Hill, M. T. & Gather, M. C. Advances in small lasers. *Nat. Photonics* **8**, 908–918 (2014).

327 41. Ma, R.-M. & Oulton, R. F. Applications of nanolasers. *Nat. Nanotechnol.* **14**, 12–22 (2019).

328 42. Wu, Y.-C. *et al.* Massively parallel delivery of large cargo into mammalian cells with light
329   pulses. *Nat. Methods* **12**, 439–444 (2015).

330 43. Lee, A. S. *et al.* Prolonged survival of transplanted stem cells after ischaemic injury via the
331   slow release of pro-survival peptides from a collagen matrix. *Nat. Biomed. Eng.* **2**, 104–113
332   (2018).

333 44. Mauranyapin, N. P., Madsen, L. S., Taylor, M. A., Waleed, M. & Bowen, W. P. Evanescent
334   single-molecule biosensing with quantum-limited precision. *Nat. Photonics* **11**, 477–481

335   (2017).

336 45. Kippenberg, T. J., Holzwarth, R. & Diddams, S. A. Microresonator-Based Optical Frequency
337   Combs. *Science (80-.).* **332**, 555–559 (2011).

338 46. Coddington, I., Newbury, N. & Swann, W. Dual-comb spectroscopy. *Optica* **3**, 414 (2016).

339

Acknowledgements

Author contributions

M.S. designed, performed and analysed laser experiments and imaging. L.W. contributed to lasing
experiments and B.C. contributed to sarcomere length measurements. I.R.M.B. and L.W. developed
refractive index fitting and peak fitting software, respectively. A.M. and M.S. prepared neonatal CM
cultures with support from G.B.M.. G.B.R. prepared isolated CMs and A.D. prepared cardiac slices
under supervision of S.J.P.. S.J.P. and M.S. designed physiological experiments in isolated CMs and
cardiac slices. C.S.T. supported the preparation of Zebrafish. P.L.A. performed two photon microscopy.
M.S. and M.C.G. conceived the project and wrote the manuscript with contributions from all authors.
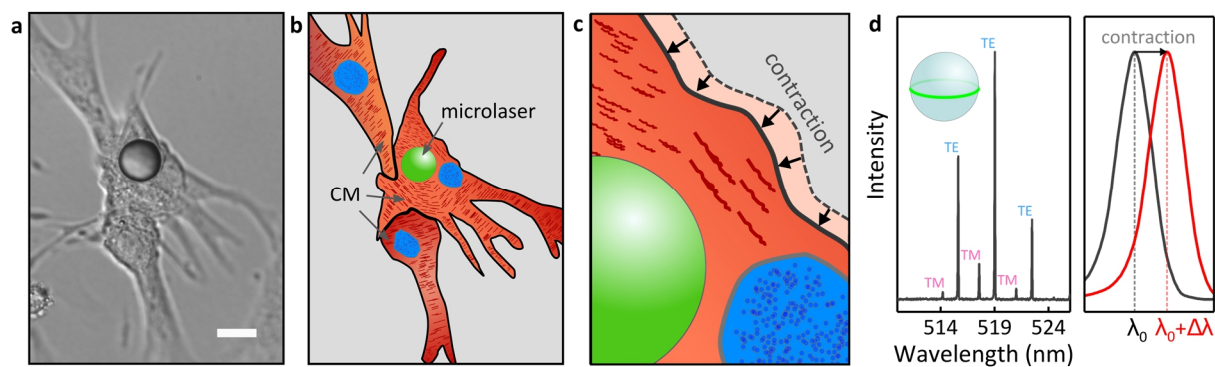
Competing interests

All authors declare no competing interests.

Additional information

Supplementary information is available for this paper at...

Correspondence and requests for materials should be addressed to M.S. and M.C.G.

365 **Figures**

366

367
368
369 **Fig. 1 | Principle of microlaser-based intracellular sensing in neonatal mouse CMs. a**, DIC microscopy and **b**,
370 schematic illustration of a group of neonatal CMs and an intracellular microlaser (green sphere). **c**, Magnified
371 view visualizing the contractile movement of the cell around the microlaser due to the action of sarcomeres
372 (dark red fibres). **d**, Measured WGM spectrum of a microlaser showing multi-mode lasing in pairs of TE- and TM-
373 modes (left). WGMs are localized within an equatorial plane close to the surface of the microlaser (inset, green
374 line). Zoom-in onto one peak in the WGM spectrum illustrating the red-shift in lasing wavelength upon CM
375 contraction (right; $\lambda_0 = 519$ nm, $\Delta\lambda = 50$ pm). Scale bar, 15 µm.

376
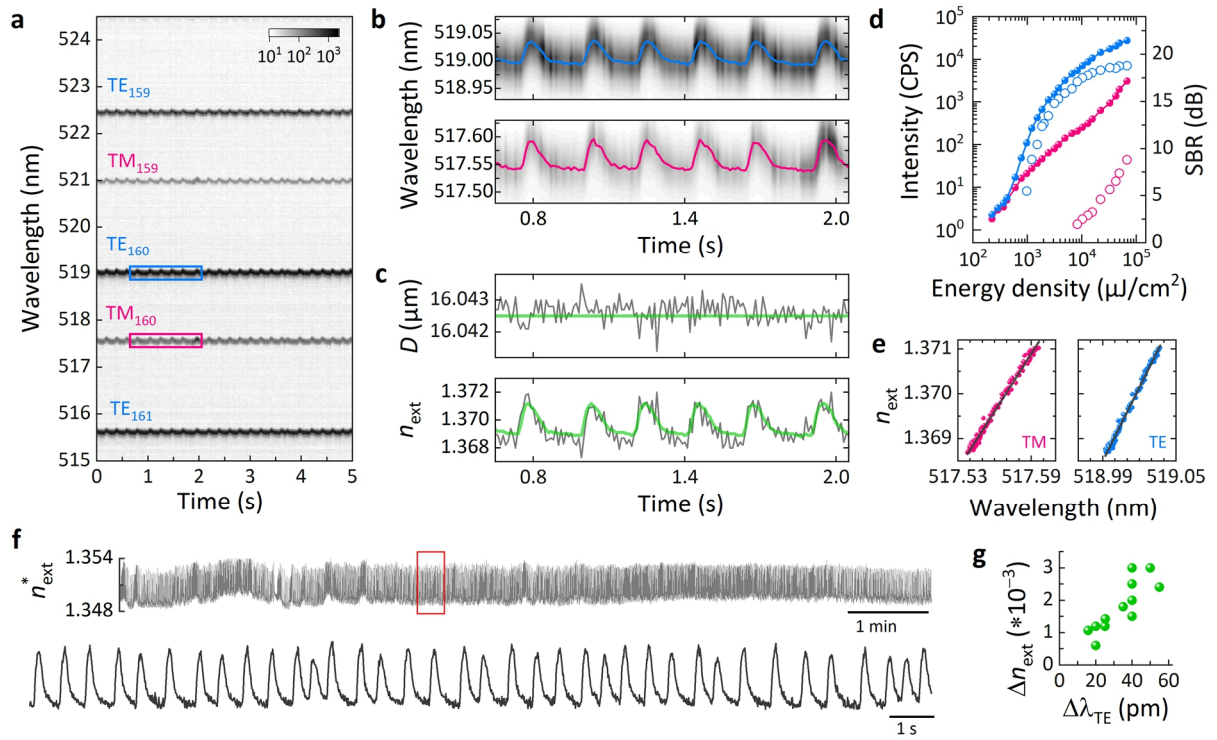
Fig. 2 | Transient red-shifts of microlaser emission are caused by changes in intracellular refractive index. a, Contour plot of the temporal evolution of the lasing spectra for an intracellular microlaser, measured with 10 ms temporal resolution. **b**, Magnified view of the areas highlighted in **a**, for a pair of TM (pink) and TE (blue) WGMs. The coloured lines show the centre position of each mode obtained from peak fitting. Shifts to longer wavelengths coincide with spontaneous CM contractions. **c**, Calculated diameter (top) of the microlaser (grey) and time-averaged diameter (green). External refractive index n_{ext} (bottom) calculated with unrestricted microlaser size (grey) and by applying the fixed mean diameter of the microlaser (green). **d**, Typical threshold characteristics (left axis, closed symbols) for the brightest TE mode (blue) and the least intense TM mode (pink) of 4 tracked lasing modes. Lasing thresholds are about 500 $\mu J/cm^2$ (TE) and 20 mJ/cm^2 (TM), respectively. Signal-to-background ratio (SBR) (right axis, open symbols) of the same modes under single pulse excitation. **e**, Mode calibration of the 2 modes shown in **b** using data from 6 contractions. From the slope of the linear fit (grey line), a sensitivity S of 0.0429 nm^{-1} and 0.0549 nm^{-1} is obtained for the TM and TE mode, respectively. **f**, Continuous single cell monitoring over 10 min (top) at 2 mJ/cm^2 (corresponding to 2 nJ/pulse) and magnified view of the 20 s window indicated by the red rectangle (bottom). **g**, Average refractive index change (Δn_{ext}) between resting phase (diastole) and peak contraction (systole) for n=12 cells plotted over the corresponding average change of the dominant TE WGM ($\Delta\lambda_{TE}$). Data representative of more than 20 independent repeats for a total of n>150 cells.

396
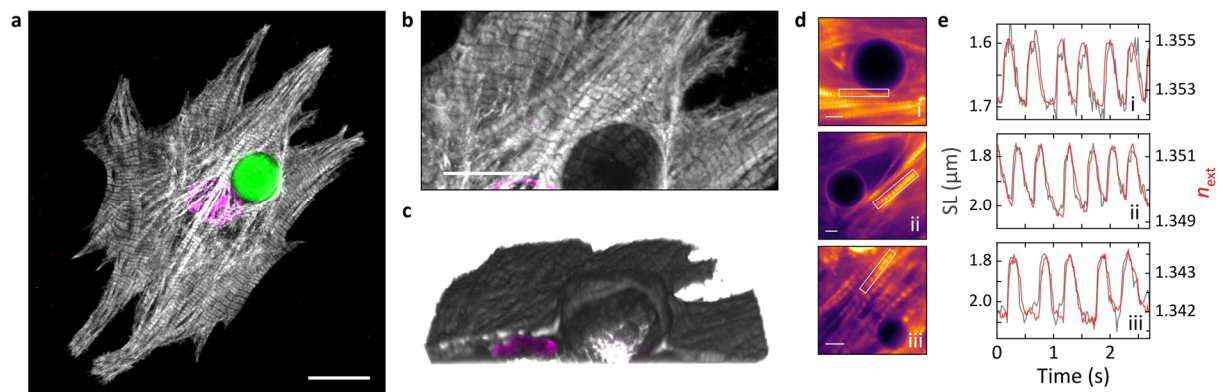
Fig. 3 | Microlasers monitor cellular contractility. 3D arrangement of myofibrils around microlasers in neonatal cardiomyocytes. **a**, Maximum intensity projection showing the sarcomeric protein cTnT (grey), cell nucleus (magenta) and microlaser (green). Scale bar, 15 µm. **b**, Magnified region around the microlaser and **c**, 3D reconstruction of the same area. The microlaser is omitted to show the arrangement of myofibrils more clearly. Scale bar, 10 µm. **d**, Video rate fluorescence microscopy (Supplementary Video 2) of neonatal mouse CMs with labelled myofibrils. Intracellular microlasers are visible as dark circular objects. Scale bars, 5 µm. **e**, Simultaneously acquired temporal profiles of sarcomere length (SL, grey, left axis, extracted from fluorescence profiles of the myofibrils highlighted by the white rectangles in **d**) and n_ext (red, right axis, extracted from microlaser spectra). Subfigures labelled according to the images in **d**.

406

407
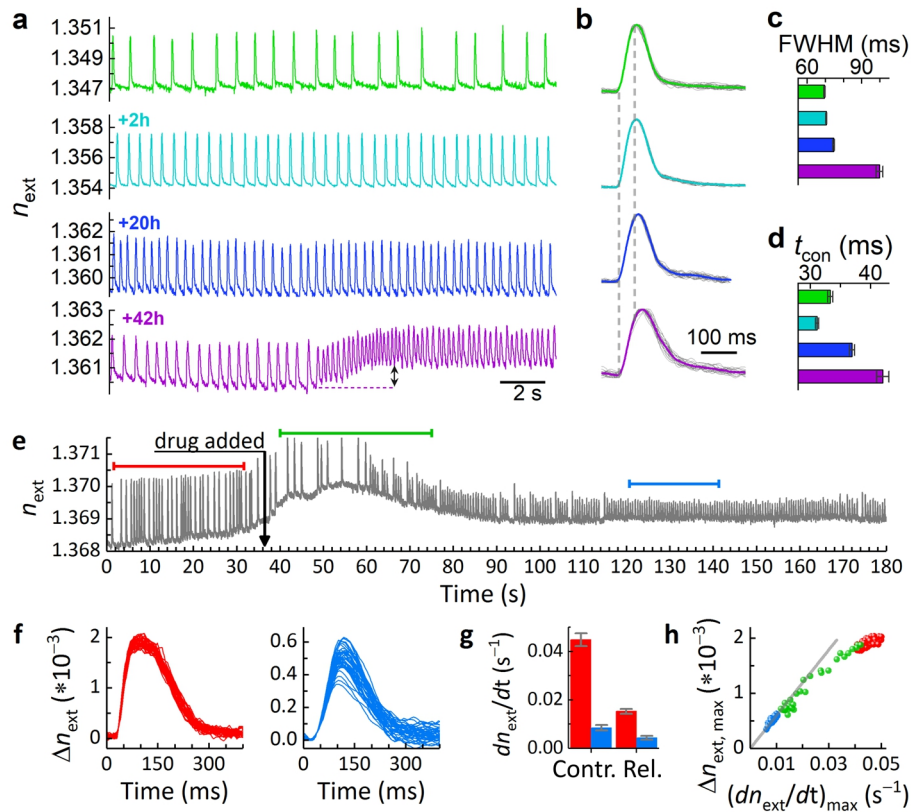
Fig. 4 | Single cell tracking and contractility sensing under compromised conditions. a-d, Microlaser-based
tracking and monitoring of a single neonatal CM. **a**, Intracellular n_{ext} trace (green) of an individual CM at start
of experiment, and characterized again after 2 h (cyan), 20 h (blue) and 42 h (violet). The black arrow marks
increased contractility during spontaneous tachycardia. **b**, Normalized n_{ext} profiles of traces shown in **a** for
n=30-40 cell contractions (grey lines), overlaid by the averaged n_{ext} profiles (coloured lines). **c**, Full-width-half-
maximum (FWHM) and **d**, average mean contraction time (t_{con}) of the beating profiles in **b**. **e-h**, Effect of
nifedipine on single cell contractility. **e**, n_{ext} trace of a spontaneously beating neonatal CM during administration
of 500 nM nifedipine (black arrow). **f**, Absolute change in refractive index (Δn_{ext}) recorded before (left, red bar
in **e**) and after (right, blue bar in **e**) administration of nifedipine. **g**, Average maximum speed of contraction
(contr.) and relaxation (rel.) for the beating profiles shown in **f**. **h**, Peak refractive index change $\Delta n_{ext, max}$
plotted as function of the maximum contraction speed with linear fit to nifedipine data. Also shown is the
intermediate region (green bar in **e**). Grey line represents linear fit to the data after equilibration of the cell (blue
spheres). All error bars represent s.e.m.

421
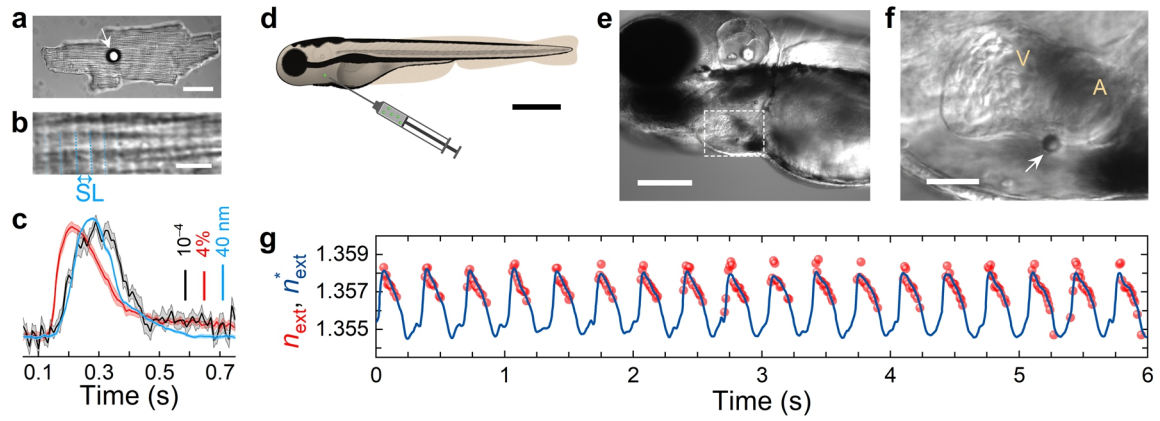
Fig. 5 | Multimodal sensing and *in vivo* integration. **a**, Extracellular microlaser (white arrow) on top of an adult CM. Scale bar, 30 µm. **b**, Magnified view showing highly organized myofibrils (sarcomere repeat units indicated by dashed blue lines). Scale bar, 4 µm. **c**, Averaged profiles of n_{ext}^* (black), SL (blue), and fluorescent calcium reporter (red). Shaded areas represent s.e.m. of at least 10 contractions. Experiments were performed in duplicate for a total of n=5 cells. **d-g**, Integration of microlaser into live zebrafish. **d**, Schematic drawing of microlaser injection. Scale bar, 500 µm. **e**, Microlaser attached to the atrium of a zebrafish heart (3 dpf). Scale bar, 200 µm. **f**, Magnified view of the microlaser (arrow). V, ventricle; A, atrium. Scale bar, 50 µm. **g**, n_{ext} (red spheres) and n_{ext}^* (blue line) calculated using sensitivity calibration. 2-4 microlasers were injected into 3 embryos and contraction signals were recorded from 3 microlasers of one embryo.

433
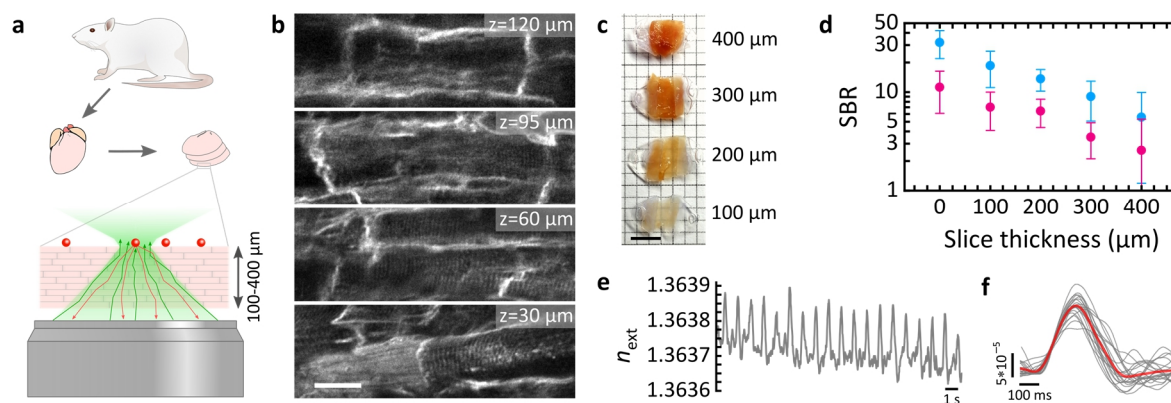
Fig. 6 | Living myocardial slices and deep tissue contractility sensing. a, Preparation of left ventricular slices from adult rat hearts. Microlasers (red spheres) were deposited on top of contracting slices. Excitation of the microlasers (green arrows illustrate combination of ballistic and diffuse pump light) through the slice and detection of the microlaser emission (red arrows) by the same objective. **b,** Two-photon microscopy images of the left ventricle at different imaging depth (z). Scale bar, 20 μm. **c**, Photograph of precision cut cardiac slices with different thicknesses. Scale bar, 5 mm. **d,** SBR of microlasers as function of slice thickness for the most (TE, blue) and least intense (TM, pink) laser modes. Error bars represent s.e.m., obtained from analysing 2 slices from 2 hearts and 20 microlasers per thickness. **e,** n_{ext} profile of a single microlaser recorded through a 350 μm thick cardiac slice that was electrically paced at 1 Hz. **f,** Overlaid profiles (grey) from **e** and average contractility profile (red). Experiments were performed in triplicate and contractility profiles have been recorded for n=11 microlasers.

Methods

Animals

The use of experimental animals was approved by the Animal Ethics Committee of the University of St Andrews and the University of Edinburgh. The care and sacrifice of animals used conformed to Directive 2010/63/EU of the European Parliament on the protection of animals used for scientific purposes as well as the United Kingdom Animals (Scientific Procedures) Act 1986.

Cell culture

HL-1 cells were cultured in Claycomb medium (Sigma-Aldrich) supplemented with 100 μM norepinephrine, 10 % (v/v) foetal bovine serum (FBS), 2 mM L-glutamine and 1 % (v/v) penicillin/streptomycin (PS). The cells were stored in T-25 flasks (Fisher Scientific) and incubated at 37°C with 5% CO_2. Prior to seeding, the flasks were coated with gelatine/fibronectin (0.02% gelatine, 1 mg/ml fibronectin) for at least an hour to improve adherence of the cells. Cells were supplied daily with 1 ml of medium per 3.5 cm^2 of culture area to maintain and maximise the contractile activity.

Isolation and culture of neonatal cardiomyocytes

Neonatal mouse hearts were obtained from postnatal day 2 – 3 C57 laboratory mice. Tissue was collected, cleaned and cut into pieces in ice-cold calcium- and magnesium-free Dulbecco's phosphate buffered saline and digested for 30 min in papain (10 units/ml; Worthington) at 37°C. Treated tissue was dissociated to a single cell suspension by gentle reverse-pipetting in cell culture medium (Dulbecco's Modified Eagle's Medium with 25 mM glucose and 2 mM Glutamax, 10 % (v/v) FBS, 1 % (v/v) non-essential amino acids, 1 % (v/v) PS). Non-disaggregated material was allowed to sediment for 2 minutes and the cell suspension pelleted by centrifugation at 200 x g for 5 min. Pelleted cells were resuspended in cell culture medium and pre-plated on an uncoated cell culture flask for 2 – 4 h to enrich cardiomyocytes through surface-attachment of fibroblasts. The cell culture medium containing unattached cells was then recovered from this flask, cardiomyocytes concentrated by centrifugation and seeded at a density of 2 x 10^5 cells per dish. Prior to seeding, culture dishes (Ibidi) were coated with 0.02 % gelatin/5 μg/ml fibronectin. Cultures were kept in a humidified incubator at 37°C, 5% CO_2, 95% air. 1 x 10^5 microlasers were added to the dish one day after seeding and incubated over night. Lasing experiments were performed within the next 1-2 days while cultures showed widespread spontaneous contractions for up to two weeks.

Isolation of adult cardiomyocytes

Adult cardiomyocytes were isolated using an adapted Langendorff-free protocol as previously described.[47] Isolation solutions used were based on a modified Tyrode's solution: EDTA buffer (in mM): 5 KCl, 130 NaCl, 0.5 NaH2PO4, 10 HEPES, 10 glucose, 5 Na-pyruvate and 5 ethylenediaminetetraaceticacid (EDTA) titrated to pH 7.8 with NaOH; Perfusion buffer (in mM): 5 KCl, 130 NaCl, 0.5 NaH2PO4, 10 HEPES, 10 glucose, 5 Na-pyruvate and 1 MgCl2 titrated to pH 7.8 with NaOH; Collagenase buffer: 35 mg collagenase type II (Worthington, USA), 50 mg BSA and 15 mg protease (type XIV, Sigma-Aldrich, UK) diluted in 30 ml of perfusion buffer.

Adult C57 mice were killed by cervical dislocation, the chest cavity rapidly opened and descending vessels severed. The right ventricle was injected with 7 ml of EDTA buffer over 1 minute to quickly clear residual blood and stop contraction. The ascending aorta was clamped in situ using haemostatic forceps and the heart excised. The heart was then submerged in EDTA buffer, with a further 10 ml injection of EDTA buffer into the left ventricle over 3 minutes. EDTA buffer was cleared by injection of 3 ml of perfusion buffer into the left ventricle. The heart was then submerged in collagenase buffer, and 30-50 ml of collagenase buffer injected into the left ventricle over 10 minutes. Digestion was taken as complete following a marked reduction in resistance to injection pressure. The digested heart was then transferred to a culture dish containing fresh collagenase buffer and trimmed of any excess non-cardiac tissue. Cardiomyocyte dissociation was completed by gentle trituration using a P1000 pipette. Enzymatic digestion was inhibited by addition of perfusion buffer containing 5 % (v/v) FBS (FBS; Thermo Fisher, UK). Isolated cardiomyocytes were reintroduced to Ca^{2+} by three rounds of 20 minutes sequential gravity settling in perfusion buffer containing 300 μM, 500 μM, and 1 mM CaCl2, respectively. Cells were stained (see below) and subsequently transferred into a culture dish (Ibidi) containing 1 mM Ca^{2+} perfusion buffer. After the cells sedimented, 1 x 10^4 microlasers were added to the dish and lasing experiments were performed within 3 hours of isolation.

Cardiomyocyte staining

Neonatal cardiomyocytes were labelled with 100 nM SiR-actin overnight. Following isolation, adult cardiomyocytes were loaded with 10 µM X-Rhod-1 AM (λ_{ex}= 580 nm, λ_{em}= 602 nm; Thermo Fisher, UK) in perfusion buffer containing 1 mM $CaCl_2$ for 45 minutes at room temperature. Cells were then washed in 1 mM Ca^{2+} perfusion buffer and left for 15 minutes at room temperature to allow de-esterification of X-Rhod-1 AM.

Microlasers

15 µm diameter polystyrene (PS)- divinylbenzene microspheres stained with Firefli Fluorescent Green (Thermo Fisher, UK, 11895052, CV<12%, excitation/emission maximum: 468 nm/508 nm) were used in all experiments, except for cardiac slices where 15.5 µm diameter PS microspheres (MicroParticles GMBH, Germany, PS-FluoRed-15.5, CV 2%, excitation/emission maximum: 530 nm/607 nm) were used.

Laser spectroscopy

All components for optical pumping and laser spectroscopy were integrated into a standard inverted fluorescence microscope (Nikon, TE2000), equipped with epi fluorescence and differential interference contrast (DIC). The output from a Q-switched diode pumped solid state laser (Alphalas) with wavelength, pulse width and repetition rate of 473 nm, 1.5 ns, and 100 Hz, respectively, was coupled into the objective via a dichroic filter and passed to the sample through either a 60x oil immersion (Nikon CFI Plan Apo VC, NA 1.4) or a 40x (Nikon, Plan Apo, NA 0.95) objective. In addition, a further 1.5x magnification was used for sarcomere length tracking. The pump laser was focussed to a 15 µm large spot and a maximum pulse energy of 5-50 nJ was used depending on resonator size and tissue scattering. Emission from the microlaser was collected by the same objective, separated from the pump light by the dichroic and passed to the camera port of the microscope. The image was relayed to a 300 mm spectrometer (Andor Shamrock 303i and Andor Newton DU970P-BVF) and a cooled sCMOS camera (Hamamatsu, Orca Flash 4.0v2) using a series of relay lenses and dichroic beam splitters. The pump laser and spectrometer were synchronized such that each spectrum corresponded to a single pump pulse (i.e. acquisition rate, 100 Hz). We note that in the single pulse excitation and single pulse collection scheme applied here the acquisition rate can be further increased by increasing both, laser repetition frequency and spectrometer acquisition rate. During lasing experiments, cells were kept in a humidified on-stage incubator system (Bioscience Tools) set to 37°C and purged with 5% CO_2, 95% air.

Laser threshold characteristics were acquired on the same setup by varying the pump power with a set of neutral density filters. Below threshold, spectra were integrated over 800 pump pulses while above threshold between 100 and 20 pump pulses were used. The Signal-to-Background ratio (SBR) is defined as:

$$\text{SBR} = \frac{I_{\text{WGM}} - I_{\text{BG}}}{I_{\text{BG}}},$$ where I_{WGM} is the laser mode peak intensity and I_{BG} is the average background intensity in a 1 nm window around the laser mode. SBR measurements were performed by integrating over only 1 pump pulse to resemble the conditions of the cardiac measurements. 100 spectra were analysed for each pump energy.

Cardiac slices were measured on the same microscope. Red-emitting microlasers were pumped by an OPA tuned to 540 nm (Ekspla, 26 ps pulse width, 1kHz repetition rate) through a 20x objective (Nikon, CFI Plan Fluor, NA 0.45). Here the acquisition rate of the spectrometer was 50 Hz. SBR was determined as above, analysing 500 spectra for each microlaser. Contractility data in thick slices were obtained by smoothing (Savitzky-Golay, 15 points, 2nd order) the fitted laser mode time traces before application of the RI fitting algorithm.

Confocal microscopy

Confocal imaging was performed on a Leica TCS SP8 laser scanning microscope with 40× and 63× oil immersion objectives. Neonatal CMs were fixed for 10 min in 4% paraformaldehyde, permeabilized with Triton X-100 (1 h) and subsequently incubated with the primary cardiac troponin T (cTnT) monoclonal antibody (over night at 4°C) (Thermo Fisher, UK, MA5-12960), the secondary Anti-Mouse IgG CF™ 594 antibody (1 h) (Sigma-Aldrich, SAB4600092), and DAPI. DAPI, microlasers and myofibrils were excited by sequentially scanned continuous wave lasers with a wavelength of 405 nm, 488 nm, and 594 nm, respectively.

Multiphoton microscopy

Imaging was carried out on a Zeiss LSM 710 confocal/multiphoton system based on a Zeiss AXIO Observer Z1 inverted microscope equipped with a Plan-Apochromat 20x NA 0.8 objective. Confocal

551   imaging used a 543 nm CW laser and multi-photon imaging a Coherent Chameleon laser tuned to
552   880 nm. The sample was stained by Langendorff perfusion of an adult rat heart with a 100 μM solution of
553   the membrane dye Di-2-ANEPEQ (PromoCell, PK-CA707-61013), for 30 min at room temperature, followed
554   by dissection of the left ventricle and subsequent imaging.[1] The power of the multiphoton laser was
555   increased with increasing imaging depth.

556 **Multimodal imaging**
557   In addition to the laser coupling spectroscopy optics, a red bandpass filter placed in the dia illumination
558   path of the microscope, a quad-edge epi-luminescence filter cube and additional band pass filters at the
559   spectrograph and camera allowed simultaneous recording of microlaser lasing spectra, and the epi-
560   fluorescence and DIC imaging of cells. Live cell imaging was performed by using an on-stage incubator
561   system.

562 **Sarcomere length measurements**
563   To determine the average sarcomere length in neonatal mouse cardiomyocytes, myofibrils were
564   fluorescently labelled with SiR-actin (see above) and videos were recorded under epi-illumination
565   conditions at 50 fps using a 60x oil immersion objective (NA 1.4). Raw fluorescence microscopy images
566   were first smoothed by removing statistical noise.[48] From the smoothed videos intensity profiles were
567   taken along individual myofibrils, covering 5 to 8 sarcomere units. Profiles were then interpolated by a
568   factor of 10, to facilitate an increase in the spatial resolution of the length measurements to about 10 nm
569   that was otherwise limited by the pixel size of the camera and magnification of the microscope.
570   Interpolated profiles were smoothed using the Savitzky-Golay method. Minima in the intensity profiles
571   were tracked through time at 20 ms intervals. Once the separation between the first and last minima was
572   determined, it was divided by the number of sarcomeres to calculate the average sarcomere length in each
573   frame. In adult cardiomyocytes, sarcomere length measurements were performed using DIC videos
574   recorded at 100 fps by using the ImageJ plugin SarcOptiM.[3] Briefly, a fast Fourier transformation algorithm
575   is used to extract the regular spacing in a line profile plotted along the longitudinal axis of the cell. Adult
576   cardiomyocytes were electrically paced at 1 Hz with Platinum wire bath electrodes by applying 8 ms square
577   voltage pulses with a maximum electric field of 30 V/cm.

578 ***In vivo* zebrafish experiments**
579   All zebrafish embryos used in our experiments were under the age of 5 days post fertilisation (dpf).
580   Embryos were collected from random matings and then correctly developmentally staged. Fertilised eggs
581   were transferred at the 2–8 cell stage to 10 cm culture dishes at 28.5°C with systems water replaced every
582   24 h. When necessary, larvae were anaesthetised with MS-222 (tricaine methanesulfonate, 40 μg/ml,
583   Sigma-Aldrich). Microlasers were injected into the sinus venosus region of 3 dpf embryos with a
584   micropipette (pulled on a Sutter P97) attached to a Narishige IM-300 microinjector, whilst viewed on a
585   stage of a Leica M16F stereo microscope. Lasing experiments were performed at room temperature.

586 **Cardiac slices**
587   Preparation of cardiac slices from rat hearts was previously described.[26,28]
588   Experimental solutions were as follows: Slicing solution (in mM) – 30 BDM, 140 NaCl, 6 KCl, 10 glucose, 1
589     $MgCl_2$, 1.8 $CaCl_2$, 23 $NaHCO_3$ titrated to 7.4 with HCl; Tyrode's solution (in mM): 140 NaCl, 5 KCl, 10 glucose,
590   1 $MgCl_2$, 2 $CaCl_2$, 23 $NaHCO_3$ titrated to 7.4 with HCl. Solutions were filtered with 0.22-micron filter
591   (Millipore) and cooled to 4°C. Carbogen gas (95% O_2/5% CO_2) was used to bubble solutions throughout the
592   preparation and slicing of the heart.
593   Adult Wistar rats were anesthetised by Pentobarbital injection, sacrificed by cervical dislocation and death
594   confirmed by carotid artery dissection. The chest cavity was opened and the vessels cut. The heart and
595   lungs were removed from the animal, submerged in cold slicing solution and blood ejected from the heart
596   by compressing for 10-15 seconds. Heart and lungs were transferred to a 10 cm dish (Fisher) filled with
597   cold slicing solution. Using a scalpel, the lungs were dissected off, followed by the atria and right ventricle.
598   An incision was made down the septum towards the apex, the ventricle opened, papillary muscles removed
599   and tissue block flattened. Excess solution was blotted from the epicardial surface, and the tissue block
600   attached to a block of 3.5% agar (3.5% agar made in dH_2O) using superglue - epicardial surface face down.
601   The agar block was then glued to the specimen holder and set in the vibratome bath so the ventricle was
602   sliced from base to apex. The vibratome bath was filled with cold slicing solution until the tissue block was
603   fully covered.

604 Slicing was carried out on Leica VT 1200 vibratome using a stainless steel blade (Wilkinson Sword) which
605 was replaced for each ventricular block. The settings were as follows: amplitude of 2 mm, blade advance
606 of 0.03 mm/s. Slice thickness was varied between 100–400 μm. Once the slice detached from the tissue
607 block, a fine brush was used to transfer the sample to a well of a 6 well plate (Fisher) filled with 4°C Tyrode's
608 solution. The slice was flattened and held down with gauze and a metal washer and the plate kept on ice.
609

610 **Data availability**

611 The research data underpinning this publication can be accessed at https://doi.org/10.17630/97927f1f-
612 a111-46d0-8d41-038771733b73.[49]

613 **Code availability**
614 The custom-made computer code is available at https://doi.org/10.17630/97927f1f-a111-46d0-8d41-
615 038771733b73.[49]
616

617 47.   Ackers-Johnson, M. *et al.* A Simplified, Langendorff-Free Method for Concomitant Isolation of
618   Viable Cardiac Myocytes and Nonmyocytes From the Adult Mouse Heart. *Circ. Res.* **119**, 909–
619   20 (2016).

620 48.   Carlton, P. M. *et al.* Fast live simultaneous multiwavelength four-dimensional optical
621   microscopy. *Proc. Natl. Acad. Sci.* **107**, 16016–16022 (2010).

622 49.   Schubert, M. *et al.* Monitoring contractility in single cardiomyocytes and whole hearts with
623   bio-integrated microlasers (dataset). *Univ. St Andrews Res. Portal* (2020)
624   doi:10.17630/97927f1f-a111-46d0-8d41-038771733b73.